



**HAL**  
open science

# Laser beam energy dependence of martensitic transformation in SLM fabricated NiTi shape memory alloy

Y. Yang, J.B. Zhan, B. Li, J.X. Lin, J.J. Gao, Z.Q. Zhang, L. Ren, P. Castany, T. Gloriant

## ► To cite this version:

Y. Yang, J.B. Zhan, B. Li, J.X. Lin, J.J. Gao, et al.. Laser beam energy dependence of martensitic transformation in SLM fabricated NiTi shape memory alloy. *Materialia*, 2019, 6, pp.100305. 10.1016/j.mtla.2019.100305 . hal-02122179

**HAL Id: hal-02122179**

**<https://univ-rennes.hal.science/hal-02122179>**

Submitted on 15 May 2019

**HAL** is a multi-disciplinary open access archive for the deposit and dissemination of scientific research documents, whether they are published or not. The documents may come from teaching and research institutions in France or abroad, or from public or private research centers.

L'archive ouverte pluridisciplinaire **HAL**, est destinée au dépôt et à la diffusion de documents scientifiques de niveau recherche, publiés ou non, émanant des établissements d'enseignement et de recherche français ou étrangers, des laboratoires publics ou privés.

# Laser beam energy dependence of martensitic transformation in SLM fabricated NiTi shape memory alloy

Y. Yang <sup>a,#</sup>, J.B. Zhan <sup>a,#</sup>, B. Li <sup>a</sup>, J.X. Lin <sup>a,\*</sup>, J.J. Gao <sup>b</sup>, Z.Q. Zhang <sup>c</sup>, L. Ren <sup>c</sup>, P. Castany <sup>b</sup>, T. Gloriant <sup>b,\*</sup>

<sup>a</sup> Key Laboratory of Optoelectronic Materials Chemistry and Physics, Fujian Institute of Research on the Structure of Matter, Chinese Academy of Sciences, Fuzhou 350002, China

<sup>b</sup> Univ Rennes, INSA Rennes, UMR CNRS 6226 ISCR, 35000, Rennes, France

<sup>c</sup> Titanium alloys department, Institute of Metal Research, Chinese Academy of Sciences, Shenyang 110016, China

\* Corresponding author: thierry.gloriant@insa-rennes.fr, franklin@fjirms.ac.cn

## Abstract

In this study, a near equiatomic NiTi alloy was fabricated by selective laser melting method (SLM). The effects of laser power and scanning speed on the tensile properties, shape memory properties and microstructure were comparatively investigated. Since the shape memory NiTi alloy can be characterized by its martensitic start phase transformation ( $M_s$  temperature) and by its critical stress inducing martensitic transformation ( $\sigma_c$ ), the evolution of these two parameters was investigated as the function of the delivered laser beam energy by differential scanning calorimetry and tensile tests. It was observed that the increase of the scanning speed under a certain laser power and the increase of the laser power under a certain laser beam energy density promote an increase of the critical stress ( $\sigma_c$ ) and a decrease of the  $M_s$  temperature. Consequently, high laser beam energy suppresses the formation of the martensitic B19' phase and therefore stabilizes the austenitic B2 phase. XRD and TEM observations confirm the dependence of the B2 and B19' phase formation with the processing parameters. On the other hand, the relationship between the  $M_s$  temperature and the critical stress  $\sigma_c$  was also plotted in good accordance with the Clausius-Clapeyron equation. Two new coefficients called "Energy Dependence Coefficient of martensitic transformation Temperature (EDCT)" and "Energy Dependence Coefficient of critical Stress (EDCS)" were defined and calculated to describe the laser beam energy dependence of the martensitic phase transformation. These two new thermodynamic coefficients are thus very suitable to establish a link between the machine parameters (through the delivered laser beam energy) and the nature of the material (through the martensitic transformation) in the NiTi alloy fabricated by SLM.

**Keywords:** SLM fabrication, NiTi shape memory alloy, laser beam energy, martensitic transformation

## 1. Introduction

Near equiatomic NiTi alloys are widely used in smart engineering areas thanks to the low stiffness, good corrosion resistance, biocompatibility and most importantly their functional properties [1, 2]. The functional properties actually include the pseudoelasticity, shape memory effect and high damping capacity which are all related to the forward and reversed martensitic transformation (MT) between the B2 austenitic phase and the B19' martensitic phase. However, such a solid phase transformation occurring in the shape memory alloys renders them difficult to process and machine. The spring back effects, burr formation and adhesion in conventional processing and machinery [3, 4] eventually lead to the non-accurate control of the geometry for final products. Selective laser melting as a kind of laser powder bed fusion additive manufacturing technology enables the deposition of powder materials layer by layer onto substrate and thus has advantages of direct forming, time and consumable save as well as the personalized design. The combination of SLM technique with the NiTi alloy is deemed as a promising potential to resolve the existing difficulties for conventional NiTi fabrication [4, 5].

Relevant researches on the selective laser melting (SLM) fabricated NiTi alloy are mainly concentrated on the processing optimization with both pre-alloying powder [6-18] and mixed pure powders [19] as starting powder materials, the measurement of martensitic transformation temperatures [6-18], the detection of the stress or strain-induced martensitic transformation from different thermomechanical conditions [10, 12, 15, 16-18], the effect of post-heat treatment [10, 12], evaluation of other functional properties such as the damping properties [6] and the fatigue behavior [13, 14]. Based on these numerous investigations, it is worth noting that it exists large discrepancies in results, especially in terms of the final mechanical properties and shape memory effects. There are two potential reasons responsible for such discrepancies. Firstly, the chemical compositions of the powders used vary. Indeed, it is well known that the Ni/Ti atomic ratio affects the MT temperatures, but also the content of oxygen, carbon and other impurities, which can be different from one study to another one depending on the manufacturing atmosphere used and the powder manufacturing technique used [20, 21]. Secondly, the main processing parameters includes the laser power, scanning speed, hatch distance and layer thickness and the diverse match of them provide a quite large manufacturing window without mentioning the inevitable effects caused by shape and size of deposited alloy. Therefore, a systematical investigation and conclusion is far away to be achieved for the selective laser melting NiTi alloy.

As the origin of functional properties of NiTi alloy, the MT indeed plays a crucial role in the final processing and optimization. That is why the MT temperatures [6-18] and the critical stress inducing the martensitic transformation [10, 12, 15, 16-18] are widely investigated by most of

researches. However, it is worth noting that the critical stress inducing the MT, which corresponds to the initial yielding stress in a tensile or compressive stress-strain curve, has not been well investigated in relationship with the MT temperatures due to the thermoelastic nature of such transformation in SLM NiTi alloys. Only Saedi *et al.* [12] reported the good agreement between the critical stress and the MT temperatures, but the corresponding stress and temperatures are measured under the circumstance of different testing temperatures. If we take into consideration that the laser beam affects greatly the mechanical and shape memory properties, the dependence of the MT of materials by the laser power and by the delivered laser energy density should be explored.

For such investigation, near equiatomic NiTi samples were fabricated by selective laser melting method in the present study. Two groups of samples fabricated with different laser powers and scanning speeds were used in order to vary the delivered laser beam energy. Microstructural investigations and martensitic transformation detections have been systematically conducted by X-ray diffraction (XRD), differential scanning calorimetry (DSC), tensile tests and transmission electron microscopy (TEM). From the results obtained, the martensitic phase transformation depending on the laser beam energy is finally discussed.

## 2. Materials and methods

The near equiatomic NiTi alloy powder, provided by AMC Powders Metallurgy Technology Company (Beijing, China), was produced through electrode induction-melting gas atomization (EIGA) from the Ni<sub>59.68</sub>Ti<sub>40.32</sub> (wt.%) ingot. The chemical composition in wt.% of the obtained alloying powder including impurities is shown in Table 1. The elemental content of titanium, nickel and iron were measured by inductively coupled plasma-atomic emission spectroscopy (ICP-AES). The content of oxygen element was determined by infrared method after fusion under inert gas. The content of carbon element was measured by high frequency combustion method with infrared measurement. It should be noticed that the atomic Ni/Ti ratio can be determined as approx. 1.21 and 1.04 for the ingot and powder, respectively. A commercial SLM machine (Mlab-R, CONCEPT LASER) was used for fulfillment of the fabricating process in an argon atmosphere (99.99%) with a constant oxygen content of 300ppm.

Two groups of samples categorized by different laser powers ( $P=60$  or  $95$  W) were selected in the present study with the aim to investigate the martensitic transformation in NiTi alloy samples fabricated with each laser power in a comparative approach. For such comparison, similar beam energy density range must be targeted and for that, the scanning speed ( $v=300\sim 850$  m/s) was varied while the hatch distance ( $h=110$   $\mu\text{m}$ ) and layer thickness ( $t=25$   $\mu\text{m}$ ) were kept constant. Therefore, according to the classical equation used:  $E=P/(v\times h\times t)$  [22-24], the value of  $E$ , which represents the

delivered laser beam energy per volume of material (energy density) during the selective laser melting process, can be calculated. Results are shown in Table 2, in which the corresponding different processing parameters are also listed. The reason for selection of such parameters is actually based on previous investigations [25, 26] which revealed that the optimum processing energy density is around 50-70 J/mm<sup>3</sup> for SLM fabrication of NiTi alloy. Thus, with the processing parameters used, it can be noted that the 60W-*x*# samples were fabricated with about the same beam energy as 95W-*x*# samples. Further, a meander pattern was used as the scanning strategy to reduce the thermal stress within layers, while the scanning angle was alternated by 90° upon the precedent layer to minimize the thermal stress between layers. To minimize the defect caused by melt splashing, the scanning direction was restricted to be always opposite to the air flow. Cubic specimens with a size of 10×10×10 mm<sup>3</sup> were deposited directly on the substrate for microstructural characterizations. Specimens were mechanically polished of about 100 μm in order to remove defects on the rough surface before testing. The Archimedes method for weighting samples in air and subsequently in alcohol (99.9%) at 25 °C was adopted to evaluate the relative density.

The mechanical properties of the SLM fabricated NiTi alloy were estimated by tensile tests with a strain rate of 10<sup>-3</sup> s<sup>-1</sup> on the INSTRON 3369 machine up to the final failure. An extensometer was used to ensure the accuracy of strain. Normalized flat tensile specimens with 5×20×2 mm<sup>3</sup> gage dimensions were directly deposited and used. The tensile direction was chosen parallel to the X direction in Fig. 1d. Each tensile test value was obtained by mathematically averaging the test results of three parallel samples.

A Netzsch DSC 200 F3 differential scanning calorimetry (DSC) with a heating/cooling rate of 10 °C/min in nitrogen atmosphere was used to evaluate the characteristic temperatures during transformation between -60 °C and 80 °C. The X-ray diffraction (XRD) was performed at room temperature for phase detection on Rigaku D-Max 2400 generator in the 2θ angle range of 35-80 ° with a scanning step of 0.01 °. The chemical composition was measured with the FEI NanoSEM450 field-emission scanning electron microscope (SEM) equipped with X-MaxN energy dispersive spectroscopy (EDS). The SLM products were observed under a Leica optical microscope (OM). The samples for OM observations were etched by the reagent composed of 3.2 % HF, 14.1 % HNO<sub>3</sub> and 82.7 % H<sub>2</sub>O in volume fraction. Further microstructure observations were conducted using a JEOL 2100 transmission electron microscope (TEM) equipped with energy dispersive X-ray spectrum operated at 200 kV. Thin foils for TEM observations were cut as disks of 3 mm in diameter, further mechanically polished to a thickness of 60 μm and then thinned by a twin-jet electro-polishing technique with a solution composed of 80% CH<sub>3</sub>OH and 20% H<sub>2</sub>SO<sub>4</sub> solution in volume. Twin-jet electro-polishing was stopped before perforation and the samples were finally

thinned by ion milling with a Fischione 1010 machine.

### 3. Results

#### 3.1 Fabrication and observation of the SLM products

The morphology of the NiTi alloy powder is shown on the SEM micrograph in Fig. 1a, where the powder displays a nearly spherical morphology. The size distribution of the powder particles (Fig. 1b) ranging from  $D_{10}=24.1 \mu\text{m}$  to  $D_{90}=54.9 \mu\text{m}$  accords with a Gaussian distribution centered on  $D_{50}=40.6 \mu\text{m}$ . The phase constitution of the powder was characterized and indexed by XRD (Fig. 1c). It can be observed that the austenitic B2 phase is solely confirmed for the powder. The control and optimization of the SLM fabrication process are performed firstly via maximizing density on the basis of the Archimedes' principle. Indeed, this process has been done at least three times for each sample and all the processing conditions and leads to a relative density higher than 99.5%. Nevertheless, these values can be slightly higher than the true value. Such difference could result from the non-accurate employment of the theoretical density ( $6.45 \text{ g/cm}^3$  for the equiatomic NiTi [27] ) used in the present case. Fig. 1d displays the macro-appearance of some NiTi cubic samples deposited on the substrate and no warping effect mentioned in previous references [4, 5] can be noticed. Due to the fact that planar defects can be formed between melting layers, which bring tiny effects on the density but probably detrimental to both static and dynamic mechanical properties, the SLM fabricated NiTi products on the X-Z plane deserves observations. Fig. 2 displays the optical microstructures of several selected SLM samples fabricated with the laser beam powers of 60 W and 95 W, respectively. It is found that microstructures are all featured with similar columnar morphologies along the building direction (Z axis in Fig. 1d) due to epitaxial growth of grains during the SLM process [28]. It should also be noticed that the microstructures of 60 W group in Fig. 2a, 2b and 2c show a darker contrast and more complex details compared with the microstructures of 95 W group in Fig. 2d, 2e and 2f. On the other hand, spherical defects are clearly visible in Fig. 2d and 2e. Concerning on the location of these spherical defects, most of them locate along the columnar grain boundaries. In order to explore the reasons of such spherical defects formation, the sample 60W-1# in Fig. 2a and 95W-1# in Fig. 2d are compared. For both of the two samples, they were fabricated with the same delivered laser energy density of  $72.7 \text{ J/mm}^3$ , more defects in Fig. 2d can be then attributed to the higher laser power. However, the sample 95W-8# in Fig. 3f was also fabricated with the same higher power value but a nearly doubled scanning speed from 475 to 850 mm/s which leads to a fewer number of spherical defects in the contrary. Therefore, it can be concluded that the occurrence of the spherical defects is not only linked with the laser

power, but also with the scanning speed. In other words, the inappropriate selection of fabricating parameter should be responsible for them.

### 3.2 Microstructural characterizations

Fig. 3 displays the XRD profiles for all samples 60W-1#~8# and 95W-1#~8#. In order to distinguish differences concerning the phase constitution, diffraction peak position for the two main B2 and B19' phases existing in the NiTi alloy are highlighted below diffraction profiles in black and red vertical solid lines. Indeed, the group of 95 W samples seems to contain only the austenitic B2 phase, while the group of 60 W sample seems to contain both austenitic B2 phase and small amount of martensitic B19' phase. Thus, the austenitic B2 phase is preferentially obtained at room temperature in both cases due to the fact that high cooling rate occurred in SLM fabricated samples.

TEM observations were further conducted to verify the phase constitution. Relevant observations were shown in Fig. 4a, 4b, 4c, 4d for the 60W-4# sample and in Fig. 4e, 4f for the 95W-4# sample. Indeed, the two samples were fabricated with the same energy density of  $60.6 \text{ J/mm}^3$  but a different match of laser power and scanning speed. The bright field images (BFI) in Fig. 4a shows the typical morphology of the 60W-4# sample. The corresponding selected area diffraction pattern (SADP) in Fig. 4b was obtained from the specific area circled in white in Fig. 4a. The indexation of the SADP indicates the incident beam is parallel to the  $[111]_{\text{B2}}$  zone axis. For the 60W-4# sample, similar morphology with Fig. 4a for austenitic B2 were observed frequently by TEM. Except the B2 phase, there is still a few amount of B19' martensite with a typical BFI in Fig. 4c and the corresponding SADP in Fig. 4d. However, once the sample 95W-4# was observed, only the B2 phase can be observed without any B19' phase. The typical morphology was shown by BFI in Fig. 4e and can be identified as B2 phase with the corresponding SADP in Fig. 4f. Such results coincide well with the XRD profiles, which reveal that the sample fabricated under 60 W contains mainly the B2 phase and small amount of B19' phase, while the sample fabricated under 95 W contains solely the B2 phase.

### 3.3 Martensitic transformation temperatures

The martensitic transformations in NiTi are described using characteristic temperatures including martensite start ( $M_s$ ), martensite finish ( $M_f$ ), austenite start ( $A_s$ ) and austenite finish ( $A_f$ ) temperatures, which can be easily detected by DSC [29]. Another two important temperatures  $M_p$  and  $A_p$  correspond to the maximum and minimum heat flow on cooling and on heating, respectively. These characteristic temperatures depend on the chemical composition, microstructure and finally

will affect the shape memory properties and mechanical responses.

All the DSC curves obtained from the present SLM fabricated NiTi alloy are presented in Fig. 5. According to the DSC curves obtained from the two groups 60 W and 95 W in Fig. 5a and 5b, respectively, the measurement of  $A_s$ ,  $A_f$ ,  $A_p$ ,  $M_s$ ,  $M_f$  and  $M_p$  can be evaluated with the method of intersection point between two tangent lines as shown in Fig. 5a. The room temperature of 25°C is highlighted by a vertical dash line. In this study, more attention is paid on the  $M_s$  values and their measurements are listed in Table 3. It can be observed that with increasing of scanning speed from bottom to top in Fig. 4a and 4b for both groups, the  $M_s$  values shift to low temperature range. Further, the  $M_s$  values for the 95W-x# samples are inferior compared with its counterpart of 60W-x# samples although the laser beam energy density is the same. This fact is also in accordance with the XRD profiles where the martensitic phase is indeed evidenced for the 60 W group but is suppressed for the 95 W group. It is still interesting to note that there are some small shoulder peaks in the DSC curves indicated by black arrows in Fig. 5. Such shoulder peaks can be ascribed by the formation of the intermediate R phase, which is regularly encountered in NiTi shape memory alloys [30, 31].

### 3.4 Tensile test results

Fig. 6 present the tensile stress-strain curves until fracture for samples fabricated under 60 W in Fig. 6a and 95 W in Fig. 6b, respectively. Each curve displays a stress plateau, which is due to the stress-induced martensitic transformation occurring in the present SLM fabricated NiTi alloy. The mechanical characteristics determined from all curves including the initial yielding stress corresponding to the critical stress inducing the martensitic transformation ( $\sigma_c$ ), the ultimate tensile strength and the failure elongation were measured. The method used to evaluate  $\sigma_c$  from the initial yielding stress is showed in this figure and corresponds to the intersection of two tangent red dash lines closed to the plateau. The values of ultimate tensile strength and failure elongation are also pointed with red dash lines. All these mechanical values obtained from Fig. 6 are listed in Table 3.

It can be observed in Table 3 that the failure elongation values are evaluated to lie between 4.7 % and 7.3 %. For the group of samples fabricated with a power of 60 W, no clear difference in the failure elongation was observed whatever the applied scanning speed. However, for the group of samples fabricated with a power of 95 W, the higher scanning speeds (samples 5#~8#) lead to comparatively lower failure elongation values. Taking the consideration of the optical microstructures in Fig. 2 in which the less spherical defects are prone to form with the higher scanning speed, one can conclude that the observed spherical defect in Fig. 2 is not the key factor to reduce the failure elongation.

Further, for both group samples, the critical stress inducing the martensitic transformation

increases with the scanning speed. The lowest and highest critical stress value corresponds to the sample 60W-1# fabricated with the lowest scanning speed of 300 mm/s and the sample 95W-8# fabricated with the highest scanning speed of 850 mm/s, respectively. Concerning the ultimate tensile strength, no trend was observed. This is because the ultimate tensile strength and failure elongation are quite dependent on the presence of defects such as micro-cracks or residual porosity in surface which strongly depend on the SLM process and the sample preparation.

#### 4. Discussion

It is clearly demonstrated in this study that the nature and the properties of the SLM fabricated NiTi shape memory alloy strongly depend on the laser power and the scanning speed. This has an important influence on the relative B2 and B19' phases stabilities. Thus, the fact that the critical stress inducing the martensitic transformation increases with the scanning speed for each group of samples fabricated with either 60 W or 95 W demonstrates an increase of the relative austenitic B2 phase stability (compared to B19') when the scanning speed rises. This observation is also corroborated by the measurements of the characteristic martensitic transformation temperatures for which a shift of values towards the lower temperatures has been observed when the scanning speed increases.

On the other hand, superior  $\sigma_c$  values and inferior  $M_s$  values for the sample 95W- $x$ # compared with its counterpart of 60W- $x$ # fabricated with the same energy density indicates a higher relative stability of the austenitic B2 phase for the sample 95W- $x$ # than the sample 60W- $x$ #. This observation is corroborated by the XRD and TEM microstructural investigations for which only the B2 phase is detected in the 95 W series while the martensitic B19' phase is also detected in the 60 W series. The reason can be attributed to the higher cooling rate, which is achieved at higher laser power. Indeed, it has already been reported in literature that the use of high laser power restricts the formation of B19' phase and therefore stabilize the B2 phase in SLM NiTi alloys [16, 32].

Owing to the unique combination of the  $M_s$  temperature and the critical stress inducing the martensitic phase transformation ( $\sigma_c$ ) for shape memory alloys fabricated with traditional method, an explicit equation accepted widely as a Clausius-Clapeyron equation can be used [33]:

$$d\sigma_c/dM_s = -\rho\Delta S/\varepsilon_t = -\rho\Delta H/T_0\varepsilon_t \quad (1)$$

Where  $\rho$  is the density of the transforming body,  $\Delta S$  the entropy change during transformation and  $\varepsilon_t$  the linear strain of the transformation in the direction of the uniaxial stress. Given that all these parameters are constants for a given transformation system, it is commonly regarded that Eq. (1) describes a linear relationship between the critical stress,  $\sigma_c$ , and the martensite start temperature,  $M_s$ .

According to the  $M_s$  values obtained from the DSC curves and the  $\sigma_c$  values evaluated by tensile tests for the present SLM fabricated NiTi samples, the  $M_s$  is plotted with respect to the critical stress  $\sigma_c$  in Fig. 7. Results show indeed a linear relationship in agreement with the Clausius-Clapeyron type equation. The exact formulas including the slope and intercept were labeled for each laser power condition in Fig. 7. It can also be observed both lines show a similar slope of approximate -0.075 K/MPa but different intercept. The same slope indicates that the relationship between the  $M_s$  temperature and the critical stress  $\sigma_c$  is independent of the laser power. One can predict the  $M_s$  with extrapolation method once the critical stress and the laser power are known, and vice versa the critical stress can be predicted according to the  $M_s$  and the laser power used. Concerning on the intercept, the difference implies the effect of the laser beam power on the  $M_s/\sigma_c$  relationship. Indeed, the lower intercept value for the group of higher laser power corresponds to the lower  $M_s$  and higher critical stress under the circumstance of the same laser beam energy density. This is in good accordance with our previous illustration and other references [16, 32, 33].

Further, in order to evaluate the effect of the laser beam energy on the martensitic transformation, the  $M_s$  temperatures and the critical stresses,  $\sigma_c$ , were plotted as the function of the delivered laser beam energies, E, in Fig. 8. As shown in this graph, linear relationships are obtained. From their slopes, two new coefficients named “Energy Dependence Coefficient on transformation Temperature (EDCT)” where  $EDCT = \Delta M_s / \Delta E$  (in  $K/J \cdot mm^{-3}$ ) and “Energy Dependence Coefficient on critical Stress (EDCS)” where  $EDCS = \Delta \sigma_c / \Delta E$  (in  $MPa/J \cdot mm^{-3}$ ) can be defined in order to evaluate the effect of the laser beam energy on the martensite start temperature and on the critical stress inducing the martensitic transformation, respectively. Based on these definitions, the EDCT are determined for each group as following:  $EDCT_{60W} = 0.495 K/J \cdot mm^{-3}$  and  $EDCT_{95W} = 0.363 K/J \cdot mm^{-3}$ , while the EDCS are determined for each group as following:  $EDCS_{60W} = -6.484 MPa/J \cdot mm^{-3}$  and  $EDCS_{95W} = -5.069 MPa/J \cdot mm^{-3}$ . The importance of the two coefficients lies on that the EDCT and EDCS characterize the increase of the  $M_s$  temperature and the decrease of the critical stress by increasing the laser beam energy unit under a certain laser power, respectively. Thus, it is demonstrated that the use of a higher laser power leads to a lower shift of the  $M_s$  temperature and to a lower shift of the critical stress. It is also interesting to notice that the ratio  $EDCT/EDCS$  should be equal to the slopes ( $dM_s/d\sigma_c$ ) in Fig. 7. Indeed, it is calculated  $EDCT_{60W} / EDCS_{60W} = -0.076 K/MPa$  and  $EDCT_{95W} / EDCS_{95W} = -0.071 K/MPa$  for 60 W and 95 W, respectively. The slopes of -0.075 K/MPa for 60 W and -0.070 K/MPa for 95 W determined from the Clausius-Clapeyron relationships coincide quite well with these  $EDCT/EDCS$  ratios. Therefore, the definition of EDCT and EDCS here, as new thermodynamic coefficients, indeed reveals the link between the nature of

the material and the processing conditions in the present SLM fabricated NiTi shape memory alloy.

## 5. Conclusion

In this study, near equiatomic shape memory NiTi samples were fabricated by selective laser melting method (SLM). Two laser powers of 60 W and 95 W coupling with different scanning speeds were applied for comparative investigation in terms of microstructure, phase stability, mechanical and shape memory properties.

- (1) XRD and TEM investigations reveal that the samples fabricated under 60 W contain mainly the austenitic B2 phase and small amount of martensitic B19' phase, while the samples fabricated under 95 W contain solely the B2 phase.
- (2) A DSC analysis was carried out in order to determine the characteristic temperatures of the B2-B19' reversible transformation. A shift of the  $M_s$  temperatures to the low temperatures for both laser powers is observed. Nevertheless, the  $M_s$  values of the samples fabricated under 95 W are inferior than those fabricated under 60W confirming thus the higher stability of the B2 phase under 95 W.
- (3) The critical stress inducing martensitic transformation, the ultimate tensile strength and the failure elongation were estimated by tensile tests. Concerning the ultimate tensile strength and the failure elongation, no trend was observed. Nevertheless, it is observed that the critical stress inducing the martensitic transformation increases with the scanning speed for both 60 W and 95 W conditions.
- (4) From the DSC and the tensile test results, the relationship between the  $M_s$  temperature and the critical stress,  $\sigma_c$ , was plotted in good accordance with the Clausius-Clapeyron equation. From the slopes,  $dM_s/d\sigma_c$  were calculated to be -0.075 K/MPa for 60 W and -0.070 K/MPa for 95 W, respectively. The same slope indicates that the relationship between the  $M_s$  temperature and the critical stress is independent of the laser power.
- (5) Two new thermodynamic coefficients EDCT (Energy Dependence Coefficient of martensitic transformation Temperature) and EDCS (Energy Dependence Coefficient of critical Stress) are defined to describe the laser beam energy dependence of the martensitic phase transformation by plotting the  $M_s$  temperatures and the critical stresses,  $\sigma_c$ , as the function of the energy density. For each laser power used the following values are determined to be:  $EDCT_{60W} = 0.495 \text{ K/J.mm}^{-3}$ ,  $EDCT_{95W} = 0.363 \text{ K/J.mm}^{-3}$ ,  $EDCS_{60W} = -6.484 \text{ MPa/J.mm}^{-3}$  and  $EDCS_{95W} = -5.069 \text{ MPa/J.mm}^{-3}$ . EDCT and EDCS coefficients characterize the decrease of the  $M_s$  temperature and the increase of the critical stress by decreasing the laser beam energy unit under a certain laser power, respectively. Thus, these

two new thermodynamic coefficients are very suitable to establish the link between the nature of the material and the processing parameters in SLM fabricated NiTi shape memory alloy.

### Declaration of interest

The work was financially supported by the National Key R&D Plan (2018YFB1105100) and by the National Science Foundation for Young Scientists of China (51801199). All authors have no financial and personal relationships with other people or organizations that could inappropriately influence (bias) their work.

Declarations of interest: none.

### Acknowledgement

The work was financially supported by the National Key R&D Plan (2018YFB1105100) and by the National Science Foundation for Young Scientists of China (51801199).

### References

- [1] K. Otsuka, X. Ren, Physical metallurgy of Ti–Ni-based shape memory alloys, *Prog. Mater. Sci.*, 50 (2005) 511-678.
- [2] Z.G. Wei, R. Sandström, S Miyazaki, Review: Shape-memory materials and hybrid composites for smart systems, *J. Mater. Sci.*, 33 (1998) 3743 - 3762.
- [3] M. Elahinia, N. Shayesteh Moghaddam, A. Amerinatanzi, S. Saedi, G.P. Toker, H. Karaca, G.S. Bigelow, O. Benafan, Additive manufacturing of NiTiHf high temperature shape memory alloy, *Scripta Mater.*, 145 (2018) 90-94.
- [4] M. Elahinia, N. Shayesteh Moghaddam, M. Taheri Andani, A. Amerinatanzi, B.A. Bimber, R.F. Hamilton, Fabrication of NiTi through additive manufacturing: A review, *Prog. Mater. Sci.*, 83 (2016) 630-663.
- [5] M.H. Elahinia, M. Hashemi, M. Tabesh, S.B. Bhaduri, Manufacturing and processing of NiTi implants: A review, *Prog. Mater. Sci.*, 57 (2012) 911-946.
- [6] X. Wang, M. Speirs, S. Kustov, B. Vrancken, X. Li, J.-P. Kruth, J. Van Humbeeck, Selective laser melting produced layer-structured NiTi shape memory alloys with high damping properties and Elinvar effect, *Scripta Mater.*, 146 (2018) 246-250.
- [7] S. Saedi, N. Shayesteh Moghaddam, A. Amerinatanzi, M. Elahinia, H.E. Karaca, On the effects of selective laser melting process parameters on microstructure and thermomechanical response of Ni-rich NiTi, *Acta Mater.*, 144 (2018) 552-560.
- [8] S. Saedi, A.S. Turabi, M.T. Andani, C. Haberland, H. Karaca, M. Elahinia, The influence of heat treatment on the thermomechanical response of Ni-rich NiTi alloys manufactured by selective laser melting, *J. Alloys. Compd.*, 677 (2016) 204-210.

- [9] S. Dadbakhsh, B. Vrancken, J.P. Kruth, J. Luyten, J. Van Humbeeck, Texture and anisotropy in selective laser melting of NiTi alloy, *Mater. Sci. Eng. A*, 650 (2016) 225-232.
- [10] S. Saedi, A.S. Turabi, M.T. Andani, N.S. Moghaddam, M. Elahinia, H.E. Karaca, Texture, aging and superelasticity of selective laser melting fabricated Ni-rich NiTi alloys, *Mater. Sci. Eng. A*, 686 (2017) 1-10.
- [11] C. Haberland, H. Meier, J. Frenzel, On the properties of Ni-rich NiTi shape memory parts produced by selective laser melting, in: *Proceedings of the ASME 2012 Conference on Smart Materials, Adaptive Structures and Intelligent Systems*, American Society of Mechanical Engineers, (2012) 97-104.
- [12] S. Saedi, A.S. Turabi, M.T. Andani, C. Haberland, M. Elahinia, H. Karaca, Thermomechanical characterization of Ni-rich NiTi fabricated by selective laser melting, *Smart Mater. Struct.*, 25 (2016) 035005.
- [13] A. Bagheri, M. J. Mahtabi, N. Shamsaei, Fatigue behavior and cyclic deformation of additive manufactured NiTi, *J. Mater. Process Tech.*, 252 (2018) 440-453.
- [14] M. Speirs, B. Van Hooreweder, J. Van Humbeeck, J.P. Kruth, Fatigue behaviour of NiTi shape memory alloy scaffolds produced by SLM, a unit cell design comparison, *J. Mech. Behav. Biomed. Mater.*, 70 (2017) 53-59.
- [15] M.T. Andani, S. Saedi, A.S. Turabi, M.R. Karamooz, C. Haberland, H.E. Karaca, M. Elahinia, Mechanical and shape memory properties of porous Ni<sub>50.1</sub>Ti<sub>49.9</sub> alloys manufactured by selective laser melting, *J. Mech. Behav. Biomed. Mater.*, 68 (2017) 224-231.
- [16] S. Dadbakhsh, M. Speirs, J. Kruth, J.V. Humbeeck, Influence of SLM on shape memory and compression behaviour of NiTi scaffolds, *CIRP Ann-Manuf. Techn.*, 64 (2015) 209-212.
- [17] N.S. Moghaddam, S.E. Saghaian, A. Amerinatanzi, H. Ibrahim, P. Li, G.P. Toker, H.E. Karaca, M. Elahinia, Anisotropic tensile and actuation properties of NiTi fabricated with selective laser melting, *Mater. Sci. Eng. A*, 724 (2018) 220-230.
- [18] J. Sam, B. Franco, J. Ma, I. Karaman, A. Elwany, J.H. Mabe, Tensile actuation response of additively manufactured nickel-titanium shape memory alloys, *Scripta Mater.*, 146 (2018) 164-168.
- [19] B. Zhang, J. Chen, C. Coddet, Microstructure and Transformation Behavior of in-situ Shape Memory Alloys by Selective Laser Melting Ti-Ni Mixed Powder, *J. Mater. Sci. Technol.*, 29 (2013) 863-867.
- [20] J. Frenzel, E.P. George, A. Dlouhy, Ch. Somsen, M.F.-X. Wagner, G. Eggeler, Influence of Ni on martensitic phase transformations in NiTi shape memory alloys, *Acta Mater.*, 58 (2010) 3444-3458.
- [21] J. Frenzel, Z. Zhang, C. Somsen, K. Neuking, G. Eggeler, Influence of carbon on martensitic phase transformations in NiTi shape memory alloys, *Acta Mater.*, 55 (2007) 1331-1341.
- [22] L. Thijs, F. Verhaeghe, T. Craeghs, J.V. Humbeeck, J.-P. Kruth, A study of the microstructural evolution during selective laser melting of Ti-6Al-4V, *Acta Mater.*, 58 (2010) 3303-3312.
- [23] L.C. Zhang, Y. Liu, S. Li, Y. Hao, Additive Manufacturing of Titanium Alloys by Electron Beam Melting: A Review, *Adv. Eng. Mater.*, (2017) 1700842.
- [24] Y.J. Liu, S.J. Li, H.L. Wang, W.T. Hou, Y.L. Hao, R. Yang, T.B. Sercombe, L.C. Zhang, Microstructure, defects and mechanical behavior of beta-type titanium porous structures manufactured by electron beam melting and selective laser melting, *Acta Mater.*, 113 (2016) 56-67.
- [25] C. Haberland, M. Elahinia, J.M. Walker, H. Meier, J. Frenzel, On the development of high quality NiTi shape memory and pseudoelastic parts by additive manufacturing, *Smart Mater. Struct.*, 23 (2014) 104002
- [26] J. Walker, C. Haberland, M.T. Andani, D. Dean, M. Elahinia, Process development and characterization of additively manufactured NiTi shape memory parts, *J. Mater. Process. Technol.*, 27 (2016) 2653-2660

- [27] J.M. Walker, C. Haberland, M. Taheri Andani, H.E. Karaca, D. Dean, M. Elahinia, Process development and characterization of additively manufactured nickel–titanium shape memory parts, *J. Inter. Mat. Syst. Str.*, 27 (2016) 2653-2660.
- [28] Gregory S. Rohrer, Grain boundary energy anisotropy: a review, *J. Mater. Sci.*, (2011) 46: 5881-5895.
- [29] H.C. Lin, S.K.Wu, J.C. Lin, The martensitic transformation in Ti-rich TiNi shape memory alloys, *Mater. Chem. Phys.*, 37 (1994) 184-190.
- [30] M. Nishida, C.M.Wayman, T. Honma, Precipitation processes in near-equiatomic TiNi shape memory alloys, *Metall. Mater. Trans. A.*, 17A (1986) 1505-1515
- [31] C.M.Wayman, S. Miyazaki, The R-phase transition and associated shape memory mechanism in Ti-Ni single crystals, *Acta Metall.*, 36 (1987) 181-192.
- [32] S. Dadbakhsh, M. Speirs, J.P. Kruth, j. Schrooten, J. Luyten, J.V. Humbeeck, Effect of SLM parameters on transformation temperatures of shape memory nickel titanium parts, *Adv. Eng. Mater.*, 16 (2014) 1140-1146.
- [33] Y. Liu, A. Mahmud, F. Kursawe, T. Nam, Effects of pseudoelastic cycling on the Clausius-Clapeyron relation for stress-induced martensitic transformation in NiTi, *J. Alloys. Compd.* 449 (2008) 82-87

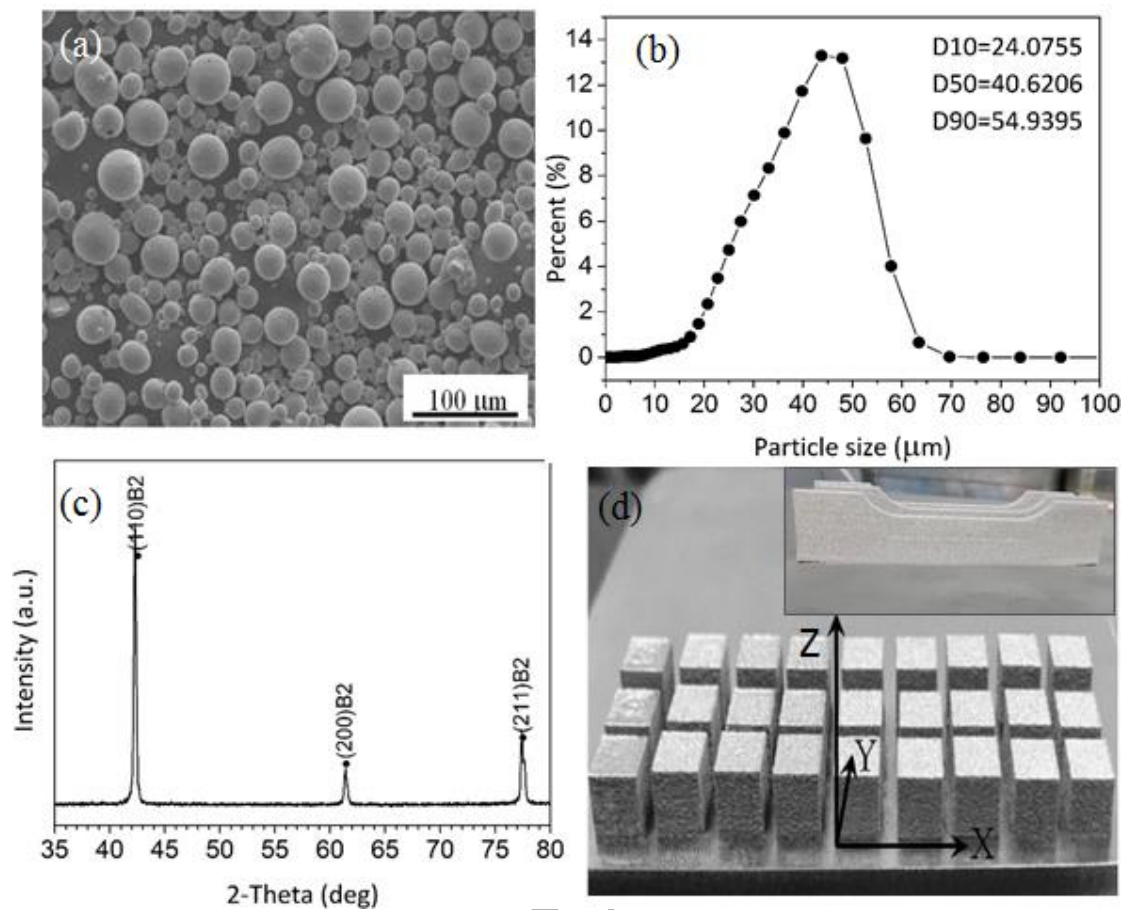


Fig. 1. (a) SEM micrograph showing the powder morphology, (b) the particle size distribution, (c) XRD diffraction profile of the NiTi powder and (d) the morphology of SLM fabricated cubes and tensile test samples.

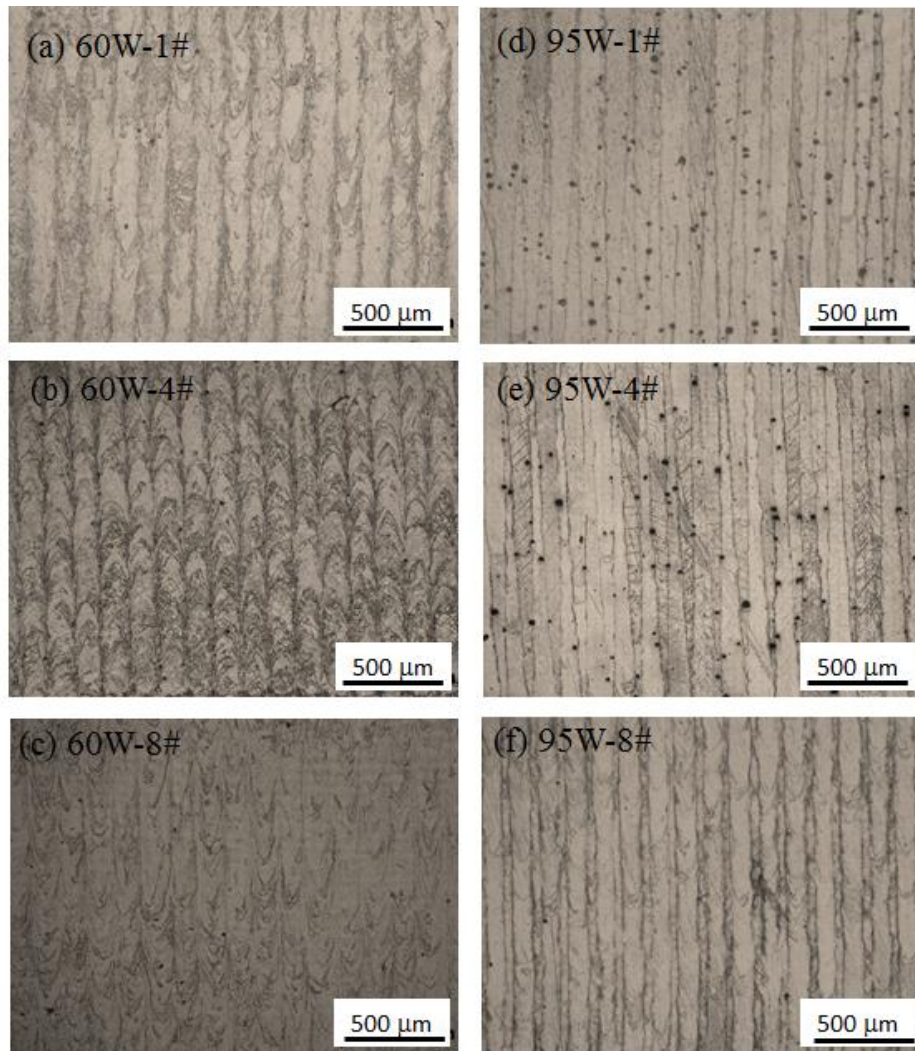


Fig. 2. Microstructures observed by optical microscopy along the building direction for NiTi alloy samples fabricated with a hatch spacing of  $110\mu\text{m}$  and a layer thickness of  $25\mu\text{m}$ , but with different laser powers and scanning speeds: (a) 60W-1#, 300 mm/s, (b) 60W-4#, 360 mm/s, (c) 60W-8#, 480 mm/s, (d) 95W-1#, 475 mm/s, (e) 95W-4#, 570 mm/s and (f) 95W-8#, 850 mm/s.

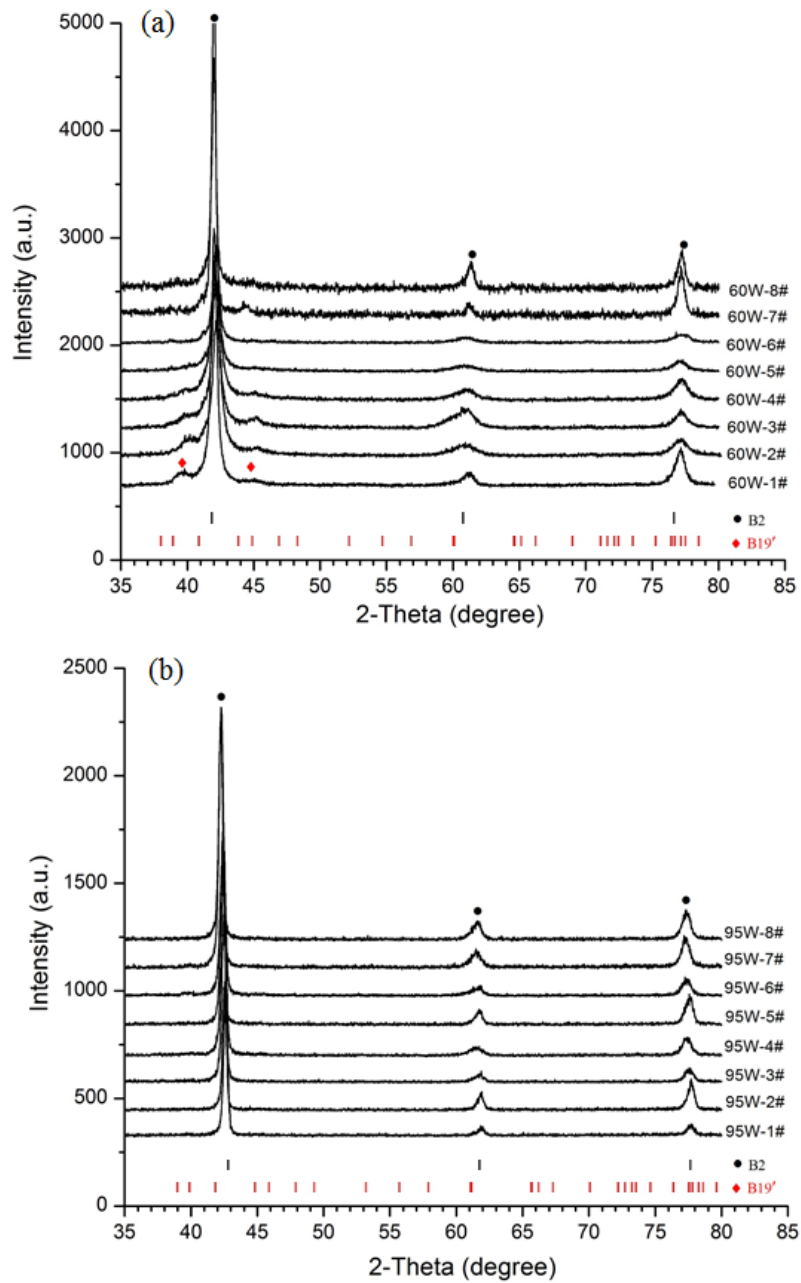


Fig. 3. XRD profiles of the different SLM fabricated samples: (a) 60 W group and (b) 95 W group

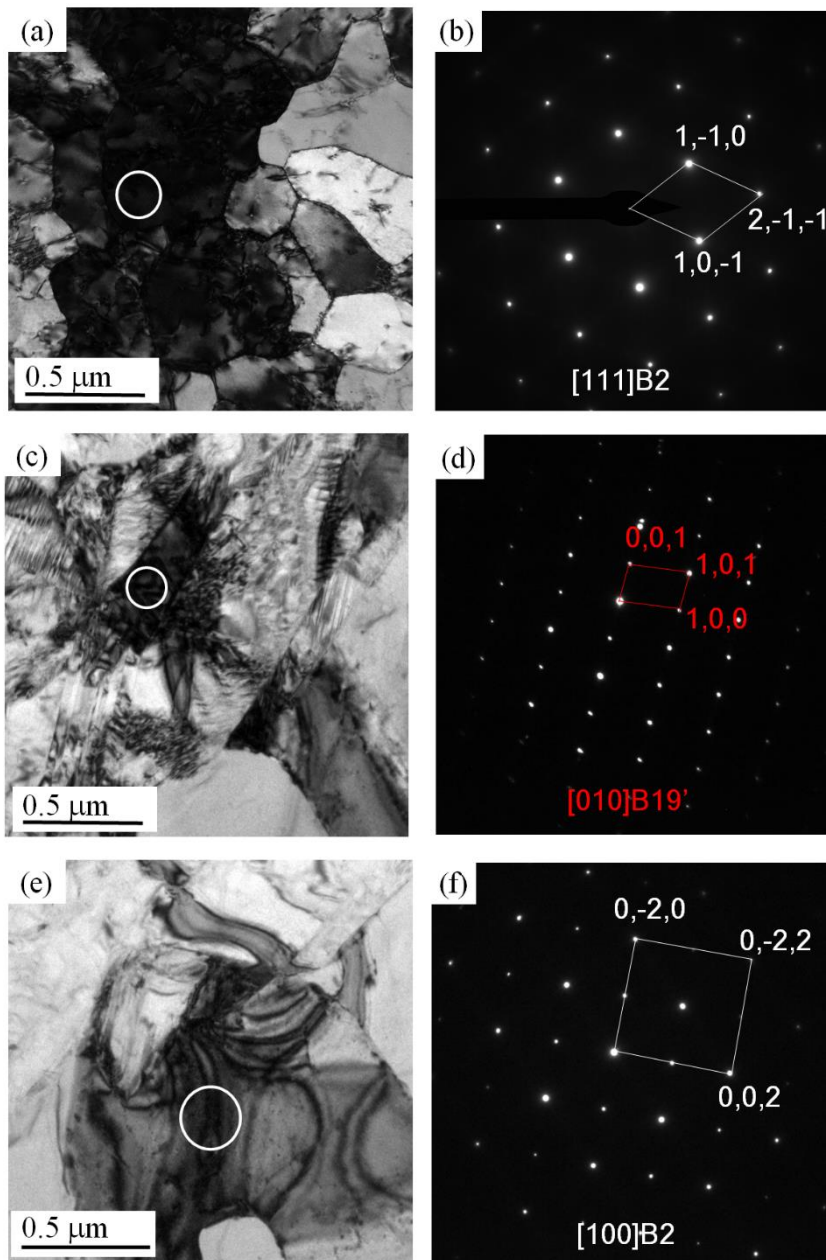


Fig. 4. TEM observations performed on the sample 60W-4# (a-d) and 95W-4# (e, f): (a) bright field image showing the B2 grains, (b) the corresponding SADP obtained from the area highlighted by white circle in (a), (c) bright field image showing the B19' martensite, (d) the corresponding SADP obtained from the area highlighted by white circle in (c); (e) bright field image showing the B2 grains and (f) the corresponding SADP obtained from the area highlighted by white circle in (e).

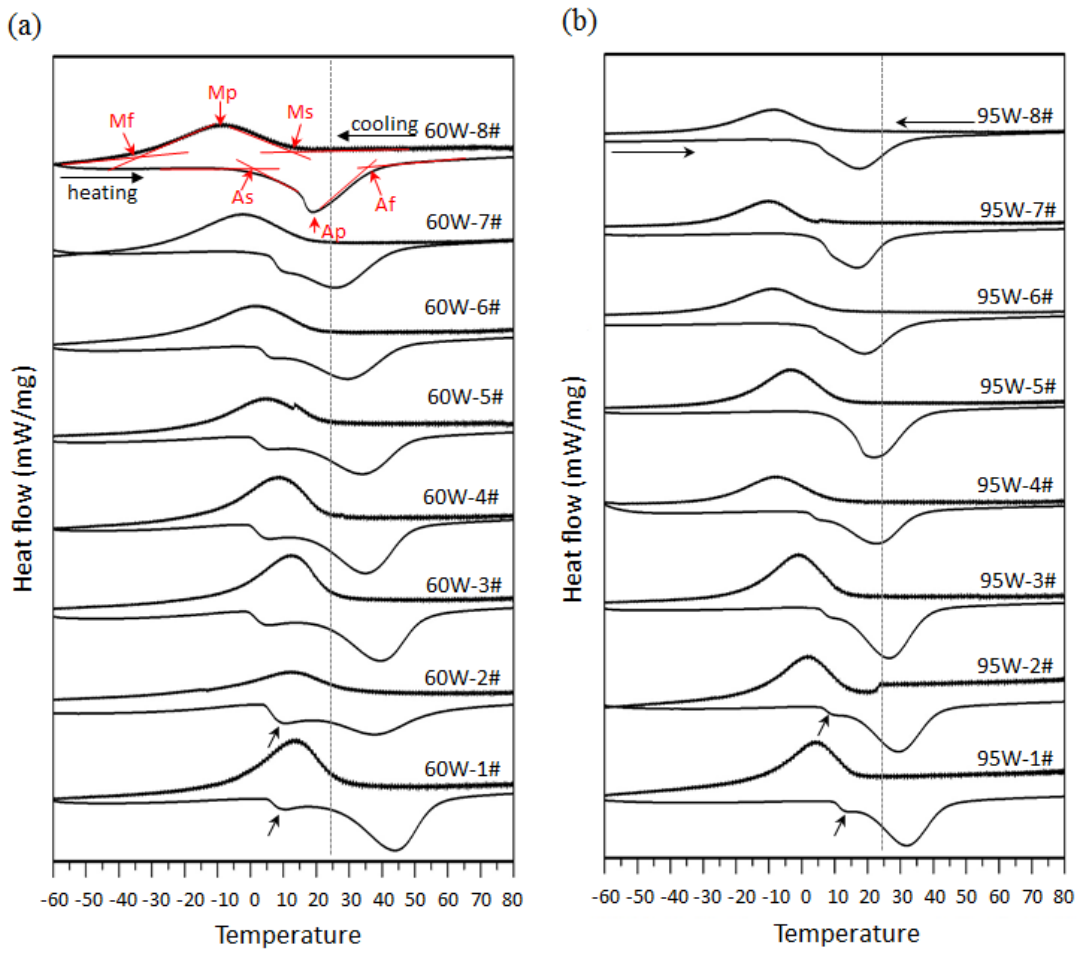


Fig. 5 DSC curves of SLM fabricated samples: (a) 60 W and (b) 95 W.  $M_s$ ,  $M_f$ ,  $A_s$  and  $A_f$  represent martensite start, martensite finish, austenite start and austenite finish temperatures, respectively. Room temperature was marked by a vertical dash line.

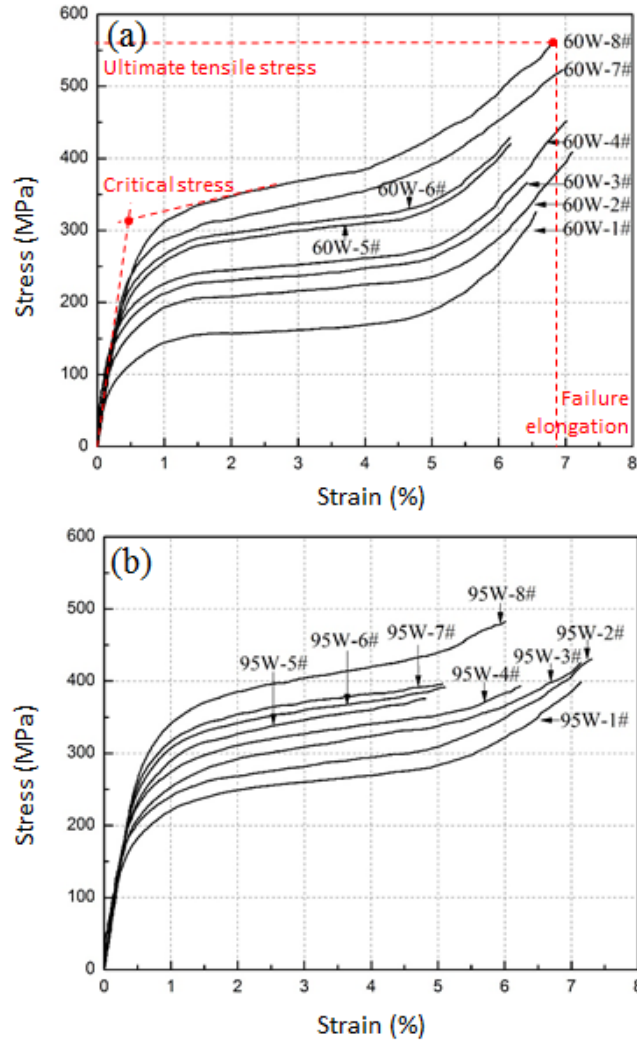


Fig. 6. Stress-strain tensile curves of SLM NiTi samples fabricated under a laser power of: (a) 60 W and (b) 95 W. The method used to measure the critical stress from the initial yielding stress is indicated with red dash lines.

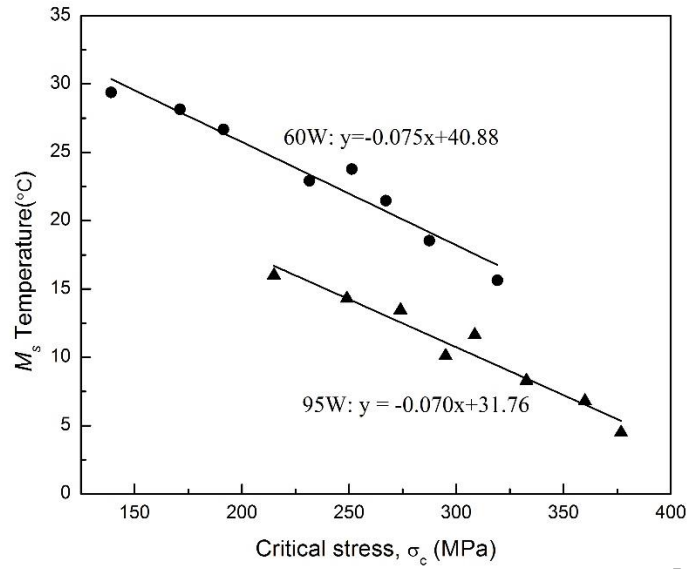


Fig. 7. Linear relationship between the  $M_s$  temperature and the critical stress,  $\sigma_c$ .

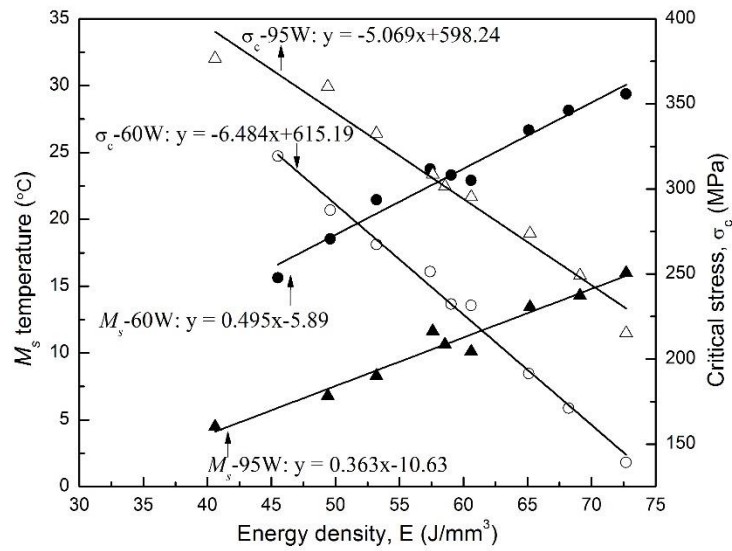


Fig. 8. Linear relationships between the  $M_s$  temperature and the laser beam energy,  $E$ , (solid symbols) and between the critical stress,  $\sigma_c$ , and the energy density,  $E$ , (open symbols).

Table 1. Chemical composition of the as-received NiTi alloy powder

| Element | Ti    | Ni    | O     | Fe    | C      |
|---------|-------|-------|-------|-------|--------|
| Wt. %   | 44.48 | 55.98 | 0.046 | 0.004 | 0.0025 |

Table 2. Processing parameters used for the different SLM fabricated NiTi alloy samples

| Number | Power (W) | Scanning speed (mm/s) | Hatch spacing (mm) | Layer thickness ( $\mu\text{m}$ ) | Energy density, E ( $\text{J}/\text{mm}^3$ ) |
|--------|-----------|-----------------------|--------------------|-----------------------------------|--|
| 60-1#  | 60        | 300                   | 110                | 25                                | 72.7   |
| 60-2#  | 60        | 320                   | 110                | 25                                | 68.2   |
| 60-3#  | 60        | 335                   | 110                | 25                                | 65.1   |
| 60-4#  | 60        | 360                   | 110                | 25                                | 60.6   |
| 60-5#  | 60        | 380                   | 110                | 25                                | 57.4   |
| 60-6#  | 60        | 410                   | 110                | 25                                | 53.2   |
| 60-7#  | 60        | 440                   | 110                | 25                                | 49.6   |
| 60-8#  | 60        | 480                   | 110                | 25                                | 45.5   |
| 95-1#  | 95        | 475                   | 110                | 25                                | 72.7   |
| 95-2#  | 95        | 500                   | 110                | 25                                | 69.1   |
| 95-3#  | 95        | 530                   | 110                | 25                                | 65.2   |
| 95-4#  | 95        | 570                   | 110                | 25                                | 60.6   |
| 95-5#  | 95        | 600                   | 110                | 25                                | 57.6   |
| 95-6#  | 95        | 650                   | 110                | 25                                | 53.2   |
| 95-7#  | 95        | 700                   | 110                | 25                                | 49.4   |
| 95-8#  | 95        | 850                   | 110                | 25                                | 40.6   |

Table 3. Martensite start temperatures and mechanical characteristics of the SLM fabricated NiTi alloy samples

| Number | $M_s$ temperature ( $^{\circ}\text{C}$ ) | Critical stress, $\sigma_c$ (MPa) | Ultimate tensile stress (MPa) | Failure elongation (%) |
|--------|--|-----------------------------------|-------------------------------|------------------------|
| 60-1#  | 29.4                                     | 139.2                             | 329.9                         | 6.6                    |
| 60-2#  | 28.2                                     | 171.2                             | 413.4                         | 7.1                    |
| 60-3#  | 26.7                                     | 191.5                             | 346.6                         | 6.4                    |
| 60-4#  | 22.3                                     | 231.6                             | 451.9                         | 7.0                    |
| 60-5#  | 23.8                                     | 251.4                             | 435.7                         | 6.1                    |
| 60-6#  | 21.5                                     | 267.3                             | 430.8                         | 6.2                    |
| 60-7#  | 18.5                                     | 287.5                             | 536.5                         | 6.9                    |
| 60-8#  | 15.6                                     | 319.2                             | 564.3                         | 6.7                    |
| 95-1#  | 16.0                                     | 215.2                             | 396.5                         | 7.1                    |
| 95-2#  | 14.3                                     | 249.1                             | 429.6                         | 7.3                    |
| 95-3#  | 13.5                                     | 273.9                             | 424.8                         | 7.1                    |
| 95-4#  | 10.1                                     | 295.3                             | 394.4                         | 6.2                    |
| 95-5#  | 11.6                                     | 308.6                             | 380.5                         | 4.7                    |
| 95-6#  | 8.3                                      | 332.7                             | 396.3                         | 5.1                    |
| 95-7#  | 6.8                                      | 360.1                             | 402.9                         | 5.0                    |
| 95-8#  | 4.5                                      | 376.8                             | 486.3                         | 6.0                    |